Physics of Fluids

Similarities between the structure functions of thermal convection and hydrodynamic turbulence

Cite as: Phys. Fluids **31**, 115107 (2019); https://doi.org/10.1063/1.5119905
Submitted: 14 July 2019 . Accepted: 27 October 2019 . Published Online: 13 November 2019

Shashwat Bhattacharya, Shubhadeep Sadhukhan, Anirban Guha, and Mahendra K. Verma

Physics of Fluids ARTICLE scitation.org/journal/phf

Similarities between the structure functions of thermal convection and hydrodynamic turbulence

Cite as: Phys. Fluids 31, 115107 (2019); doi: 10.1063/1.5119905
Submitted: 14 July 2019 • Accepted: 27 October 2019 •
Published Online: 13 November 2019

Shashwat Bhattacharya,[1,a)] Shubhadeep Sadhukhan,[2] Anirban Guha,[3] and Mahendra K. Verma[2]

AFFILIATIONS

[1] Department of Mechanical Engineering, Indian Institute of Technology Kanpur, Kanpur 208016, India
[2] Department of Physics, Indian Institute of Technology Kanpur, Kanpur 208016, India
[3] School of Science and Engineering, University of Dundee, Dundee DD1 4HN, Scotland, United Kingdom

[a)] **Electronic mail:** shabhatt@iitk.ac.in

ABSTRACT

In this paper, we analyze the scaling of velocity structure functions of turbulent thermal convection. Using high-resolution numerical simulations, we show that the structure functions scale similar to those of hydrodynamic turbulence, with the scaling exponents in agreement with the predictions of She and Leveque ["Universal scaling laws in fully developed turbulence," Phys. Rev. Lett. **72**, 336–339 (1994)]. The probability distribution functions of velocity increments are non-Gaussian with wide tails in the dissipative scales and become close to Gaussian in the inertial range. The tails of the probability distribution follow a stretched exponential. We also show that in thermal convection, the energy flux in the inertial range is less than the viscous dissipation rate. This is unlike in hydrodynamic turbulence where the energy flux and the dissipation rate are equal.

I. INTRODUCTION

Turbulence remains largely an unsolved problem for scientists and engineers even today. The energetics of three-dimensional homogeneous and isotropic turbulence is, however, well understood and was explained by Kolmogorov.[1,2] Here, the energy supplied at large scales cascades down to intermediate scales and then to dissipative scales. The rate of energy supply equals the energy flux, Π_u, and the viscous dissipation rate ϵ_u. Kolmogorov showed that such flows exhibit the following property:[1–3]

$$\left\langle \left[\{\mathbf{u}(\mathbf{r}+\mathbf{l}) - \mathbf{u}(\mathbf{r})\} \cdot \hat{\mathbf{l}} \right]^3 \right\rangle = -\frac{4}{5}\Pi_u l, \qquad \Pi_u = \epsilon_u, \tag{1}$$

for $\eta \ll l \ll L$, where L is the length scale at which energy is supplied and is of the order of the domain size, and η is the dissipative scale, called Kolmogorov length scale. In Eq. (1), $\langle\cdot\rangle$ represents the ensemble average, and $\mathbf{u}(\boldsymbol{r})$ and $\mathbf{u}(\boldsymbol{r}+\boldsymbol{l})$ are the velocity fields at positions $\mathbf{r}$ and $\mathbf{r}+\mathbf{l}$, respectively. The left-hand side of Eq. (1), denoted as $S_3^u(l)$, is the third-order velocity structure function. For any order q, one expects that, using dimensional analysis, $S_q^u(l) = \langle [\{\mathbf{u}(\mathbf{r}+\mathbf{l}) - \mathbf{u}(\mathbf{r})\} \cdot \hat{\mathbf{l}}]^q \rangle \sim l^{q/3}$. Using the theory of Obukhov[4] and Corrsin[5] on turbulence with passive scalar θ, dimensional analysis yields $S_q^\theta(l) \sim l^{q/3}$, where $S_q^\theta(l) = \langle \{\theta(\mathbf{r}+\mathbf{l}) - \theta(\mathbf{r})\}^q \rangle$ is the structure function for the passive scalar. The aforementioned relations for S_q^u and S_q^θ are known as Kolmogorov-Obukhov (KO) scaling in the literature. In reality, however, the exponents deviate from $q/3$ (other than for 3) due to intermittency effects. The velocity structure functions scale as $S_q^u(l) \sim l^{\zeta_q}$, where the exponents ζ_q fit well with the model of She and Leveque.[6]

The scaling of structure functions of turbulent convection, however, remains an unsolved problem and hence is the theme of this paper. We focus on Rayleigh-Bénard Convection (RBC) that deals with a fluid enclosed between two horizontal plates, with the bottom plate kept at a higher temperature than the top plate. In thermal convection, complications arise due to anisotropy introduced by gravity and also because the temperature T is an active scalar.

For stably stratified turbulence, Bolgiano[7] and Obukhov[8] predicted the kinetic energy spectrum $E_u(k)$ and the thermal energy

spectrum $E_T(k)$ to scale as $k^{-11/5}$ and $k^{-7/5}$, respectively, where $k \sim 1/l$ is the wavenumber. An extension of Bolgiano-Obukov (BO) theory to structure functions gives $S_q^u(l) \sim l^{3q/5}$ and $S_q^T(l) \sim l^{q/5}$, where S_q^T is the temperature structure function. BO scaling occurs above the Bolgiano length scale l_B, where the buoyancy forces are dominant. Evidences of BO scaling have been observed in recent studies of stably stratified[9,10] and rotating stratified turbulence.[11] Using theoretical arguments, Procaccia and Zeitak,[12] L'vov,[13] L'vov and Falkovich,[14] and Rubinstein[15] proposed the applicability of BO scaling to RBC as well. Researchers have attempted to confirm the above theory with the help of experiments and numerical simulations as well as using theoretical arguments.

Benzi *et al.*[16,17] simulated both 2D and 3D RBC using the lattice Boltzmann method and computed velocity and temperature structure functions up to the sixth order. They could not observe any discernible scaling for the structure functions due to short inertial range. They found them, however, to be self-similar for a wide range of l, a phenomenon known as extended self-similarity (ESS).[18,19] Furthermore, they claimed BO scaling from the relationship between the velocity and the temperature structure functions. Ching[20] computed temperature and velocity structure functions of thermal convection using the experimental data of Heslot, Castaing, and Libchaber[21] and Sano, Wu, and Libchaber[22] as well as the numerical data of Benzi *et al.*[23] Although Ching[20] observed two distinct scaling regimes separated by the Bolgiano scale, the scaling exponents deviated from BO theory.

Many researchers obtained KO scaling in the bulk and attributed it to the large value of local l_B, which is of the same order as the box size. Since l_B is small near the walls, it is argued that the structure functions in those regions follow BO scaling. Using the third-order structure functions calculated using their lattice Boltzmann simulation data, Calzavarini, Toschi, and Tripiccione[24] claimed BO scaling near the walls and KO scaling at the cell center. High-resolution multipoint measurements of velocity and temperature fields in water were conducted by Sun, Zhou, and Xia.[25] Their exponents of velocity structure functions computed at the cell center fit well with the She-Leveque model, with the lower orders following Kolmogorov scaling. Using the refined similarity hypothesis, Ching *et al.*[26] derived power-law relations for conditional velocity and temperature structure functions computed at the given values of the locally averaged thermal dissipation rate. Ching *et al.*[26] further computed the conditional temperature structure functions up to the fourth order using the experimental data of He and Tong.[27] Based on the observed power-law scaling, they concluded BO scaling near walls and KO scaling at the cell center.

Using the experimental data of Castaing *et al.*[28] and Shang *et al.*,[29] Ching[30] computed the structure functions of plume velocity and found them to scale similar to the temperature structure functions. This is unlike the case of velocity structure functions in BO scaling, where they scale differently from the temperature structure functions. Kunnen *et al.*[31] conducted direct numerical simulations (DNS) of RBC in a grid resolution of $129 \times 257 \times 257$. The velocity structure functions computed by them follow BO scaling for Rayleigh number $\mathrm{Ra} = 10^8$ and Kolmogorov scaling for higher Ra. Ching and Cheng[32] calculated temperature structure functions using the shell model of homogeneous RBC and found them to deviate significantly from BO scaling for $q > 4$. Kaczorowski and Xia[33] conducted direct numerical simulations (DNS) of RBC in grids ranging from 64^3 to 770^3 and found that the velocity structure functions computed at the cell center approach Kolmogorov scaling for lower orders.

From the conflicting nature of past results, it is clear that the behavior of the structure functions of turbulent convection has not yet been clearly established. Lohse and Xia[34] reviewed the experimental, numerical, and theoretical results of past works critically and raised doubts on the applicability of BO scaling in RBC. Recently, using phenomenological arguments and numerical simulations, Kumar, Chatterjee, and Verma[9] and Verma, Kumar, and Pandey[10] showed the Kolmogorov energy spectrum in RBC. Using energetics arguments, they derived that the energy cascade rate in turbulent convection is constant, leading to Kolmogorov scaling. Their predictions are being accepted and acknowledged by several groups as is evident from recent literature.[35–41] However, some researchers still believe that BO scaling is applicable to RBC.[11,42–44] In this paper, using numerical simulations, we reinforce the results of Kumar, Chatterjee, and Verma[9] and Verma, Kumar, and Pandey[10] by showing that the velocity structure functions of thermal convection scale similarly as those of 3D hydrodynamic turbulence. We further show that although the energy flux in turbulent convection is constant similar to hydrodynamic turbulence, it differs from the viscous dissipation rate. We will discuss the scaling of temperature structure functions in a future work.

The outline of this paper is as follows: In Sec. II, we describe the governing equations of RBC. In Sec. III, we discuss the phenomenology of turbulent convection and derive the scaling of third-order structure functions. In Sec. IV, we briefly discuss the simulation details and the procedure employed to calculate the velocity structure functions. In Sec. V, we present the scaling of the structure functions and discuss the nature of the probability distribution functions (PDFs) of velocity increments. Furthermore, we compare the energy flux and viscous dissipation rate in RBC and show that the flux is less than the dissipation rate. Finally, we conclude in Sec. VI.

II. GOVERNING EQUATIONS

In RBC, under the Boussinesq approximation,[45,46] we assume the kinematic viscosity ν, thermal diffusivity κ, and thermal expansion coefficient α to be constants. Furthermore, the density of the fluid is taken to be constant, except for the buoyancy term in the momentum equation. The temperature field T can be split as

$$T(x, y, z) = T_c(z) + \theta(x, y, z), \tag{2}$$

where $T_c(z)$ is the conduction temperature profile and $\theta(x, y, z)$ is the deviation of temperature from the conduction state. Furthermore, the temperature fluctuation θ is related to the density fluctuation ρ as[45,47]

$$\rho = -\rho_0 \alpha \theta,$$

where ρ_0 is the mean fluid density. The governing equations of RBC are as follows:

$$\frac{\partial \mathbf{u}}{\partial t} + (\mathbf{u} \cdot \nabla)\mathbf{u} = -\frac{\nabla \sigma}{\rho_0} + \alpha g \theta \hat{z} + \nu \nabla^2 \mathbf{u}, \tag{3}$$

$$\frac{\partial \theta}{\partial t} + (\mathbf{u} \cdot \nabla)\theta = \frac{\Delta}{d} u_z + \kappa \nabla^2 \theta, \tag{4}$$

$$\nabla \cdot \mathbf{u} = 0, \tag{5}$$

where $\mathbf{u}$ and σ are the velocity and the pressure fields, respectively, and Δ and d are the temperature difference and distance, respectively, between the top and the bottom plates.

Using d as the length scale, $\sqrt{\alpha g \Delta d}$ as the velocity scale, and Δ as the temperature scale, we nondimensionalize Eqs. (3)–(5), which yields

$$\frac{\partial \mathbf{u}}{\partial t} + \mathbf{u}\cdot\nabla\mathbf{u} = -\nabla\sigma + \theta\hat{z} + \sqrt{\frac{\mathrm{Pr}}{\mathrm{Ra}}}\nabla^2\mathbf{u}, \tag{6}$$

$$\frac{\partial \theta}{\partial t} + \mathbf{u}\cdot\nabla\theta = u_z + \frac{1}{\sqrt{\mathrm{Ra}\,\mathrm{Pr}}}\nabla^2\theta, \tag{7}$$

$$\nabla\cdot\mathbf{u} = 0, \tag{8}$$

where $\mathrm{Ra} = \alpha g \Delta d^3/(\nu\kappa)$ is the Rayleigh number and $\mathrm{Pr} = \nu/\kappa$ is the Prandtl number. The Rayleigh and Prandtl numbers are the main governing parameters of RBC.

In Sec. III, we construct a phenomenology for the structure functions of turbulent convection.

III. PHENOMENOLOGY FOR TURBULENT CONVECTION BASED ON HYDRODYNAMIC TURBULENCE

A. Energy fluxes and spectra in hydrodynamic turbulence and thermal convection

For 3D hydrodynamic turbulence, the energy cascade rate Π_u in turbulent flows is constant in the inertial range ($\eta \ll l \ll L$). Dimensional analysis gives the following relation for the energy spectrum $E_u(k)$:

$$E_u(k) = K_{\mathrm{KO}}(\Pi_u)^{2/3}k^{-5/3}, \tag{9}$$

where K_{KO} is the Kolmogorov constant. The aforementioned $k^{-5/3}$ spectrum is known as Kolmogorov's spectrum. In this section, we briefly describe the phenomenological arguments of Kumar, Chatterjee, and Verma,[9] Verma, Kumar, and Pandey,[10] and Verma[47] according to which the energy spectrum in turbulent convection follows Kolmogorov scaling with constant energy flux, contrary to the arguments of L'vov[13] and L'vov and Falkovich,[14] who proposed Bolgiano-Obukhov scaling with variable flux.

In all turbulent flows, the following equation can be derived using Eq. (3) (see Refs. 3, 47, and 48):

$$\frac{\partial}{\partial t}E_u(k,t) = -\frac{\partial}{\partial k}\Pi_u(k,t) + \hat{\mathcal{F}}(k,t) - \hat{D}_u(k,t), \tag{10}$$

where $\hat{\mathcal{F}}(k,t)$ is the energy feed due to forcing and $\hat{D}_u(k)$ is the dissipation rate of kinetic energy. For a steady state, we have $\frac{\partial}{\partial t}E_u(k,t) \approx 0$ that modifies Eq. (10) to

$$\frac{d}{dk}\Pi_u(k) = \hat{\mathcal{F}}(k) - \hat{D}_u(k). \tag{11}$$

Now, we will separately consider hydrodynamic turbulence and RBC and show that the flux is constant for both the cases. However, there is a difference between the two fluxes, as shown below.

1. Hydrodynamic turbulence

The forcing in hydrodynamic turbulence is supplied at small wavenumbers. In the inertial range, $\hat{\mathcal{F}}(k) = 0$ and $\hat{D}_u(k)$ is negligible. This results in the following[1–3,48] equation:

$$\frac{d}{dk}\Pi_u(k) = 0, \quad \Rightarrow \Pi_u(k) = \text{constant}. \tag{12}$$

Note that in hydrodynamic turbulence, the forcing injection $\mathcal{F}(k)$ is modeled numerically in many ways (refer to Ref. 49 for details).

Let us consider a small wavenumber k_0 that lies in the inertial range and is slightly larger than the forcing wavenumber. Integration of Eq. (11) from 0 to k_0 yields

$$\Pi_u(k_0) - \Pi_u(0) = \int_0^{k_0}\hat{\mathcal{F}}(k)dk - \int_0^{k_0}\hat{D}_u(k)dk. \tag{13}$$

Note that $\int_0^{k_0}\hat{\mathcal{F}}(k)dk$ is the total energy injection rate for hydrodynamic turbulence. Since $\Pi_u(0) = 0$ and the dissipation at small wavenumbers is negligible, we obtain

$$\Pi_u(k_0) \approx \int_0^{k_0}\hat{\mathcal{F}}(k)dk. \tag{14}$$

Now, integration of Eq. (11) from k_0 to ∞ yields

$$\Pi_u(\infty) - \Pi_u(k_0) = \int_{k_0}^{\infty}\hat{\mathcal{F}}(k)dk - \int_{k_0}^{\infty}\hat{D}_u(k)dk. \tag{15}$$

Since $\Pi_u(\infty) = 0$ and $\hat{\mathcal{F}}(k) = 0$ for $k \in [k_0, \infty)$, we get

$$\Pi_u(k_0) = \int_{k_0}^{\infty}\hat{D}_u(k)dk \approx \int_0^{\infty}\hat{D}_u(k)dk = \epsilon_u. \tag{16}$$

Note that k_0 is small and $\hat{D}_u(k)$ is small in the forcing band. Therefore, the lower limit of the aforementioned integration has been replaced with 0. Thus, using Eqs. (14) and (16), we deduce that in hydrodynamic turbulence, the energy flux in the inertial range is constant and is approximately equal to the dissipation rate ϵ_u and the total energy injection rate.

2. Thermal convection

In turbulent convection, the energy is injected into the system by buoyancy. We denote this energy feed as $\hat{\mathcal{F}}_B(k)$. Note that we do not inject energy externally in convection as we do in hydrodynamic turbulence. Furthermore, unlike hydrodynamic turbulence, $\hat{\mathcal{F}}_B(k)$ acts at all scales in thermal convection. Replacing $\hat{\mathcal{F}}(k)$ with $\hat{\mathcal{F}}_B(k)$, we rewrite Eq. (11) as

$$\frac{d}{dk}\Pi_u(k) = \hat{\mathcal{F}}_B(k) - \hat{D}_u(k). \tag{17}$$

Since hot plumes ascend and the cold plumes descend, u_z and θ are positively correlated, which means that[9,10]

$$\langle\theta(\mathbf{r})u_z(\mathbf{r})\rangle > 0.$$

Using this condition, Kumar, Chatterjee, and Verma[9] and Verma, Kumar, and Pandey[10] claimed that $\hat{\mathcal{F}}_B(k) > 0$, that is, buoyancy feeds energy to the system. Hence, $\frac{d}{dk}\Pi_u(k) > 0$ in the steady state from Eq. (17). It is important to note that in stably stratified flows, buoyancy depletes energy from the system. Thus, for such flows, $\hat{\mathcal{F}}_B < 0$, resulting in $\frac{d}{dk}\Pi_u(k) < 0$. This means that the flux decreases with wavenumber in the inertial range; this is an important ingredient of Bolgiano-Obukhov scaling.[7,8] Since the flux does not decrease with wavenumber in thermal convection, Bolgiano-Obukhov scaling is ruled out.

Furthermore, in turbulent convection, Pandey and Verma[50] and Pandey *et al.*[51] showed that buoyancy is strong only at large scales and is weak in the inertial range. Nath *et al.*[52] showed that the distribution of velocity field in turbulent convection is nearly

isotropic similar to hydrodynamic turbulence, again indicating weak buoyancy.

Based on the above observations, Kumar, Chatterjee, and Verma[9] and Verma, Kumar, and Pandey[10] argued that $\hat{\mathcal{F}}_B$ does not bring about a noticeable increase in $\Pi_u(k)$ (see Fig. 1). Therefore, $\hat{\mathcal{F}}_B \approx \hat{D}_u \approx 0$, which reduces Eq. (17) to

$$\frac{d}{dk}\Pi_u(k) \approx 0, \quad \Rightarrow \Pi_u(k) \approx \text{constant}. \tag{18}$$

Thus, it can be inferred from Eq. (18) that Kolmogorov's theory of hydrodynamic turbulence is also applicable to thermal convection. Integrating Eq. (17) from 0 to a small wavenumber k_0 lying in the inertial range yields

$$\Pi_u(k_0) - \Pi_u(0) = \int_0^{k_0} \hat{\mathcal{F}}_B(k)dk - \int_0^{k_0} \hat{D}_u(k)dk. \tag{19}$$

Since $\Pi_u(0) = 0$ and the dissipation rate is negligible at small wavenumbers, the above equation reduces to

$$\Pi_u(k_0) \approx \int_0^{k_0} \hat{\mathcal{F}}_B(k)dk. \tag{20}$$

Since $\hat{\mathcal{F}}_B(k)$ is strong at large scales, we deduce from Eq. (20) that a large part of energy is injected by buoyancy at large scales that contributes to the energy flux in the inertial range; this feature is similar to hydrodynamic turbulence.

There is, however, a difference between the energetics of RBC and that of 3D turbulence. Integrating Eq. (17) from k_0 to ∞ yields

$$\Pi_u(\infty) - \Pi_u(k_0) = \int_{k_0}^{\infty} \hat{\mathcal{F}}_B(k)dk - \int_{k_0}^{\infty} \hat{D}_u(k)dk. \tag{21}$$

Since $\Pi_u(\infty) = 0$, the above equation becomes

$$\Pi_u(k_0) = \int_{k_0}^{\infty} \hat{D}_u(k)dk - \int_{k_0}^{\infty} \hat{\mathcal{F}}_B(k)dk. \tag{22}$$

Since k_0 is small compared to the dissipation range wavenumbers, we can write

$$\int_{k_0}^{\infty} \hat{D}_u(k)dk \approx \int_0^{\infty} \hat{D}_u(k)dk = \epsilon_u.$$

Now, $\int_{k_0}^{\infty} \hat{\mathcal{F}}_B(k)dk$ is the energy injected by buoyancy at small scales. It must be noted that $\int_{k_0}^{\infty} \hat{\mathcal{F}}_B(k)dk > 0$ in RBC because $\hat{\mathcal{F}}_B(k)$, albeit weak, is positive and adds up to a significant amount when integrated over the inertial and dissipation range (see Sec. V C). Therefore,

$$\Pi_u(k_0) \approx \epsilon_u - \int_{k_0}^{\infty} \hat{\mathcal{F}}_B(k)dk < \epsilon_u. \tag{23}$$

Equation (23) clearly shows that unlike in hydrodynamic turbulence, the energy flux in the inertial range is smaller than the dissipation rate due to the energy injected by buoyancy at small scales. Recall that in hydrodynamic turbulence, no energy is injected in these regimes. In Sec. V C, using the results of numerical simulations of turbulent convection, we show that the energy flux is smaller than the dissipation rate by a factor of two to three for our selected cases. Note that this factor likely depends on Ra, Pr, type of boundary conditions, etc. A careful study of the spectra and fluxes of thermal convection for different regimes of Ra and Pr needs to be carried out to ascertain how this factor depends on the aforementioned parameters.

In Subsection III B, following the procedure of Kolmogorov,[1,2] we derive the relation for the third-order velocity structure functions of turbulent convection.

B. Velocity structure functions of turbulent convection

Sun, Zhou, and Xia[25] and Zhou, Sun, and Xia[53] performed experiments of turbulent thermal convection and observed isotropy in regions away from walls. Using detailed numerical simulations, Nath *et al.*[52] computed the modal energy of the inertial-range Fourier modes of turbulent convection as a function of polar angle Θ (angle between the buoyancy direction and the wavenumber) and found it to be approximately independent of Θ. Thus, they showed that turbulent convection is nearly isotropic. In Sec. V A, we compute the second-order velocity structure functions as functions of l and Θ (Θ is the angle between the buoyancy direction and l) using our numerical data and show that they are nearly independent of Θ. This again shows near-isotropy in thermal convection. We believe that isotropy is related to the fact that in turbulent convection, buoyancy "effectively" injects energy at large scales, but it is weak in the inertial range.

Furthermore, at high Rayleigh numbers, the boundary layers are very thin, with the boundary layer thickness $\delta_u \ll d$, where d is the domain height. Therefore, for simplification, we neglect the effects of boundary layers and consider the system to be homogeneous. In the Appendix, we show that in turbulent thermal convection, the planar structure functions and those computed in the

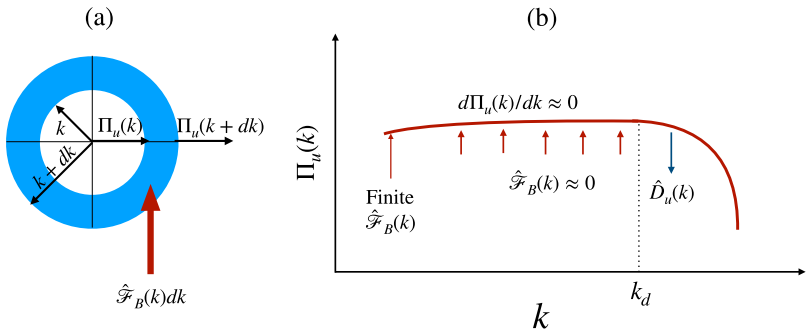

FIG. 1. For RBC: (a) A schematic diagram of a wavenumber shell of radius k showing the buoyant energy feed $\hat{\mathcal{F}}_B$ and the kinetic energy flux $\Pi_u(k)$. (b) Schematic plot of $\Pi_u(k)$ vs k. $\Pi_u(k) \approx$ constant in the inertial range because of weak $\hat{\mathcal{F}}_B$. Viscous dissipation $\hat{D}_u(k)$ is dominant for $k > k_d$.

entire domain exhibit somewhat similar scaling; this result also validates the assumptions of approximate homogeneity and isotropy for turbulent convection. Using the assumptions of homogeneity, isotropy, and steady state and following similar lines of arguments as Kolmogorov,[1,2] we derive the relation for the third-order structure function for turbulent convection in the following discussion.

For homogeneous and incompressible turbulent flows, the temporal evolution of the second-order velocity correlation function can be written as follows:[1–3]

$$\frac{\partial}{\partial t}\left[\frac{1}{2}\langle u_i(\mathbf{r})u_i(\mathbf{r}+\mathbf{l})\rangle\right] = T_u(\mathbf{l}) + \mathcal{F}_B(\mathbf{l}) - D_u(\mathbf{l}), \tag{24}$$

where

$$T_u(\mathbf{l}) = \frac{1}{4}\nabla_l \cdot \left\langle [u(\mathbf{r}+\mathbf{l}) - u(\mathbf{r})]^2 [\mathbf{u}(\mathbf{r}+\mathbf{l}) - \mathbf{u}(\mathbf{r})]\right\rangle,$$
$$\mathcal{F}_B(\mathbf{l}) = \langle F_i(\mathbf{r})u_i(\mathbf{r}+\mathbf{l})\rangle,$$
$$D_u(\mathbf{l}) = \nu\nabla'^2\langle u_i(\mathbf{r})u_i(\mathbf{r}+\mathbf{l})\rangle.$$

Here, $T_u(\mathbf{l})$ is the nonlinear energy transfer at scale $\mathbf{l}$, $\mathcal{F}_B(\mathbf{l})$ is the force correlation at $\mathbf{l}$, and $D_u(\mathbf{l})$ is the corresponding dissipation rate. The symbol ∇'^2 represents the Laplacian at $\mathbf{r}+\mathbf{l}$. Under a steady state, the left-hand side of Eq. (24) disappears. Furthermore, we focus on the inertial range where $D_u(\mathbf{l}) \approx 0$ that yields

$$\mathcal{F}_B(\mathbf{l}) \approx -T_u(\mathbf{l}). \tag{25}$$

Now, $\mathcal{F}_B(\mathbf{l})$ can be expanded as Fourier series as follows:

$$\mathcal{F}_B(\mathbf{l}) = \sum_{\mathbf{k}} \hat{\mathcal{F}}_B(\mathbf{k}) \exp(i\mathbf{k}\cdot\mathbf{l}). \tag{26}$$

Following Verma, Kumar, and Pandey,[10] we model $\hat{\mathcal{F}}_B(\mathbf{k})$ as[3]

$$\hat{\mathcal{F}}_B(\mathbf{k}) = \frac{A}{2}(\delta_{\mathbf{k},\mathbf{k}_0} + \delta_{\mathbf{k},-\mathbf{k}_0}) + Bk^{-5/3}. \tag{27}$$

Substitution of Eq. (27) into Eq. (26) yields

$$\mathcal{F}_B(\mathbf{l}) = A\cos(\mathbf{k}_0\cdot\mathbf{l}) + \int Bk^{-5/3}\exp(i\mathbf{k}\cdot\mathbf{l})d\mathbf{k}$$
$$\approx A + DBl^{2/3}. \tag{28}$$

This is because $\mathbf{k}_0\cdot\mathbf{l} \approx 0$ since turbulent convection is essentially forced by large-scale plumes.[10] Here, B is a small constant. Now, for an isotropic flow, $T_u(\mathbf{l}) = T_u(l)$ and is related to the third-order structure function $S_3^u(l)$ as (see Ref. 3)

$$T_u(l) = \frac{1}{12}\frac{1}{l^2}\frac{d}{dl}\left[\frac{1}{l}\frac{d}{dl}\{l^4 S_3^u(l)\}\right]. \tag{29}$$

Combining Eqs. (25), (28), and (29), we get

$$-\frac{1}{12}\frac{1}{l^2}\frac{d}{dl}\left[\frac{1}{l}\frac{d}{dl}\{l^4 S_3^u(l)\}\right] = A + DBl^{2/3}. \tag{30}$$

Integrating the above expression twice and noting that $S_3^u(0) = 0$, we obtain the following relation:

$$S_3^u(l) = -\frac{4}{5}(Al + D'Bl^{5/3}). \tag{31}$$

Now, we assume that the large-scale buoyant energy feed at $k = k_0$ equals the energy flux Π_u and that B is small. Therefore, we have $A \approx \Pi_u$, and

$$S_3^u(l) = -\frac{4}{5}\Pi_u l. \tag{32}$$

Thus, the scaling of the third-order structure functions of RBC is similar to those of 3D hydrodynamic turbulence, except that ϵ_u of $S_3^u(l)$ is replaced by Π_u. Note that $\Pi_u < \epsilon_u$ for RBC. We will verify the above relation in Sec. V using numerical simulations.

It is important to note that for hydrodynamic turbulence, $\hat{\mathcal{F}}(k)$ is provided at small wavenumbers and is equal to the viscous dissipation rate ϵ_u. Inverse Fourier transform of $\hat{\mathcal{F}}(k)$ results in a constant value of $\mathcal{F}(l)$ that equals ϵ_u. Using the same procedure as shown above, one can derive that $S_3^u(l) = -(4/5)\epsilon_u l$. Note that in RBC, ϵ_u of the above $S_3^u(l)$ is replaced by Π_u. We also remark that our arguments are consistent with the results of Kunnen and Clercx,[54] who computed the scale-by-scale energy budget in direct numerical simulations of RBC and showed that $S_3^u(l) \neq -(4/5)\epsilon_u l$ for convective turbulence.

Finally, as mentioned previously, it must be noted that Eq. (32) has been derived under the assumption of homogeneity and isotropy, which may not be the case for all regimes of turbulent convection. For example, Nath *et al.*[52] have shown that anisotropy is stronger for large Prandtl numbers. Thus, we cannot make the assumption of isotropy in this regime.

In Sec. IV, we discuss the numerical techniques involved in the computation of the structure functions.

IV. NUMERICAL METHODS

We use two sets of numerical data to compute the velocity structure functions, each set having different boundary conditions. The first set is the data of Verma, Kumar, and Pandey,[10] who performed direct numerical simulations (DNS) of RBC on a 4096^3 grid. The grid corresponds to a cube of unit dimension. The Rayleigh and Prandtl numbers were chosen as 1.1×10^{11} and unity, respectively. The simulation was performed using a pseudospectral code.[55,56] Free-slip and isothermal boundary conditions were employed at the top and bottom plates, and periodic boundary conditions were employed at the side walls. For details, refer to Ref. 10.

The second set of data is that of Kumar and Verma.[57] This simulation was performed using a finite volume solver[58] on a nonuniform 256^3 grid that corresponds to a cube of unit dimension. The Rayleigh and Prandtl numbers were chosen as 1×10^8 and unity, respectively. No-slip boundary conditions were imposed at all the walls; such realistic boundary conditions capture the wall effects. Isothermal boundary conditions were imposed at the top and bottom plates and adiabatic boundary conditions at the side walls. For spatial discretization schemes, time-marching method, and the validation of the code, see Refs. 57, 59, and 60. We interpolate the velocity fields to a uniform 256^3 grid.

We compute the velocity structure functions in the entire domain using a combination of shared (OpenMP) and distributed memory [Message Passing Interface (MPI)] parallelization (see Ref. 61). The computations involve running six nested for loops: the outer three loops describing the position vector $\mathbf{r}$ and the inner three loops describing $\mathbf{r}+\mathbf{l}$. To save computational resources, we condense our free-slip data to 512^3 grid. Note that we are interested only in scales pertaining to the inertial range and not the dissipative scales. After the aforementioned coarsening, we are still able to resolve scales above 6η and capture the inertial range very well in addition to avoiding unnecessary computational costs. The number

of MPI nodes used was equal to the number of grid points in the x-direction, while the number of OpenMP threads used was 32.

In Sec. V, we will discuss the numerical results.

V. NUMERICAL RESULTS

In this section, for turbulent thermal convection, we describe the scaling of the velocity structure functions, the probability distribution functions of velocity increments, and the difference between the energy flux and viscous dissipation rate.

A. Structure functions

Before computing the structure functions, we first numerically compute the viscous dissipation rate ϵ_u using the velocity field data of our free-slip and no-slip cases. We use the relation

$$\epsilon_u = \langle 2\nu S_{ij} S_{ij} \rangle \tag{33}$$

to compute the viscous dissipation rate, where S_{ij} is the strain rate tensor, and $\langle \cdot \rangle$ represents the volume average. Furthermore, we compute the Kolmogorov length scale η and the Nusselt number Nu using the following relations:[3,34,62]

$$\eta = \left(\frac{\nu^3}{\epsilon_u} \right)^{1/4}, \tag{34}$$

$$\mathrm{Nu} = 1 + \frac{\langle u_z \theta \rangle}{\kappa \Delta d^{-1}}. \tag{35}$$

In Table I, we list the values of Nu, ν, ϵ_u, and η for both free-slip and no-slip data. Clearly, η is larger for the no-slip case because of lower Ra. Furthermore, we remark that the viscous boundary layers are thin for our data, with $\delta_u = 0$ for the free-slip simulation and $\delta_u \approx 2\eta$ for the no-slip simulation.[59] Thus, most of the flow resides in the bulk.

Next, we validate the assumption of isotropy in turbulent convection. Using both sets of data, we compute the second-order velocity structure functions in the entire domain as functions of l and Θ, where Θ is the angle between the buoyancy direction and l. Figures 2(a) and 2(b) exhibit the polar plots $S_2^u(l, \Theta)$, with l spanning the inertial-dissipation range ($0 < l/\eta < 210$ for the free-slip case and $0 < l/\eta < 40$ for the no-slip case). Figures 2(a) and 2(b) clearly show that the structure functions are nearly independent of Θ, thereby demonstrating near-isotropy in the inertial-dissipation range.

Now, we compute the magnitude of S_q^u as a function of l in the entire domain, with q ranging from 2 to 10. Figure 3 exhibits the plots of structure functions of orders 2, 3, 6, 8, and 10 vs l/η for both sets of data. Contrary to the results of Benzi *et al.*,[16,17] we observe a discernible scaling range for the third order structure function. The range is found to be $32 < l/\eta < 200$ for the free-slip data and $19 < l/\eta < 40$ for the no-slip data. The range is much smaller for the no-slip case because of the higher value of η. Note that the length scales in the inertial range are much larger than the boundary layer thickness.

TABLE I. For the two simulations of RBC: Rayleigh number Ra, Nusselt number Nu, kinematic viscosity ν, viscous dissipation rate ϵ_u, and Kolmogorov length scale η.

Case	Ra	Nu	ν	ϵ_u	η
Free-slip	1.1×10^{11}	582	3.02×10^{-6}	2.59×10^{-3}	3.21×10^{-4}
No-slip	1.0×10^{8}	32.8	1.00×10^{-4}	3.18×10^{-3}	4.21×10^{-3}

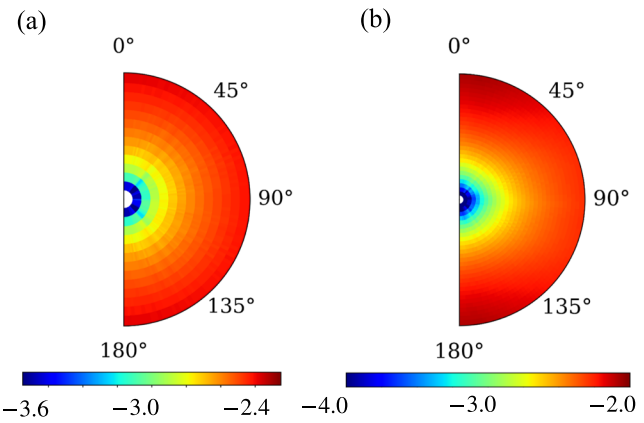

FIG. 2. For the (a) free-slip and (b) no-slip simulations of RBC: Polar (l, Θ) plots of the logarithms of second-order velocity structure functions, where Θ is the angle between the buoyancy-direction and l. l spans the inertial-dissipation range: $0 < l/\eta < 210$ for the free-slip data and $0 < l/\eta < 40$ for the no-slip data. The structure functions are nearly independent of Θ, thus demonstrating near-isotropy in the inertial-dissipation range.

We compute the scaling exponents ζ_q and the prefactor $\mathcal{A}$ by fitting the relation $S_q^u(l) = \mathcal{A} l^{\zeta_q}$ to our data within the scaling range. Table II lists $\mathcal{A}$ and ζ_q for both sets of data. Note that $\zeta_3 = 0.97$ and 0.98 for the free-slip and the no-slip cases, respectively, which are close to Kolmogorov scaling of $S_3^u \sim l$. From Table II and Figs. 3 and 4, we observe that for lower orders, the scaling exponents ζ_q for free-slip and no-slip boundary conditions are nearly equal, and they are close to $q/3$, which is a generalization of Kolmogorov's theory of turbulence. For $q = 2$, $\zeta_2 \approx 2q/3$ that yields $k^{-5/3}$ energy spectrum. These results are consistent with the Kolmogorov energy spectrum in thermal convection observed by Kumar, Chatterjee, and Verma,[9] Verma, Kumar, and Pandey,[10] and Kumar and Verma.[57] Our results are also consistent with those of Sun, Zhou, and Xia[25] and Kaczorowski and Xia,[33] who reported Kolmogorov scaling of the structure functions of RBC computed at the cell center. On the other hand, our results are contrary to those of Benzi *et al.*,[16,17] Calzavarini, Toschi, and Tripiccione,[24] and Kunnen *et al.*[31] (for $\mathrm{Ra} = 10^8$), who deduced Bolgiano-Obukhov scaling based on their simulations. However, it must be noted that Kunnen *et al.*[31] could not observe Bolgiano-Obukhov scaling for $\mathrm{Ra} > 10^8$; rather, they reported Kolmogorov scaling, similar to our results. We will discuss more on Bolgiano-Obukhov scaling later in this section.

As illustrated in Table II and Fig. 4, higher order ζ_q's for the free-slip data are marginally lower than those for the no-slip data. Also, for higher order structure functions, ζ_q deviates from $q/3$ due to intermittency. To explain intermittency effects in hydrodynamic turbulence, She and Leveque[6] proposed the following model for ζ_q:

$$\zeta_q = \frac{q}{9} + 2\left(1 - \left(\frac{2}{3}\right)^{q/3}\right). \tag{36}$$

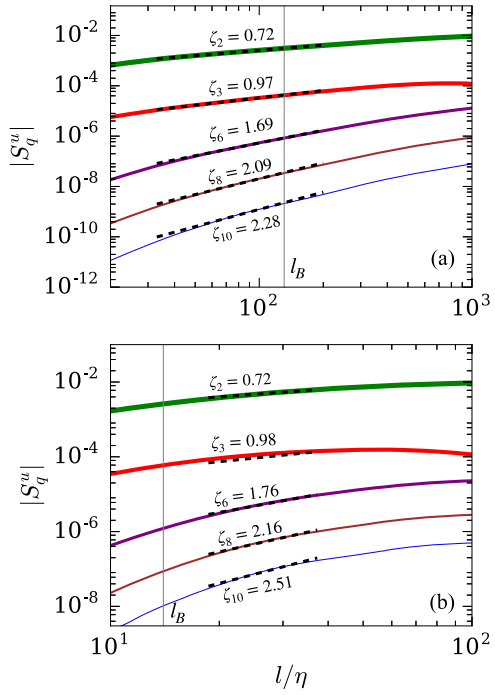

FIG. 3. For (a) the free-slip and (b) no-slip simulations of RBC: plots of $|S_q^u|$ with decreasing line thickness for q = 2 (green), 3 (red), 6 (purple), 8 (brown), and 10 (blue) vs l/η. The vertical solid gray line marks the Bolgiano length scale.

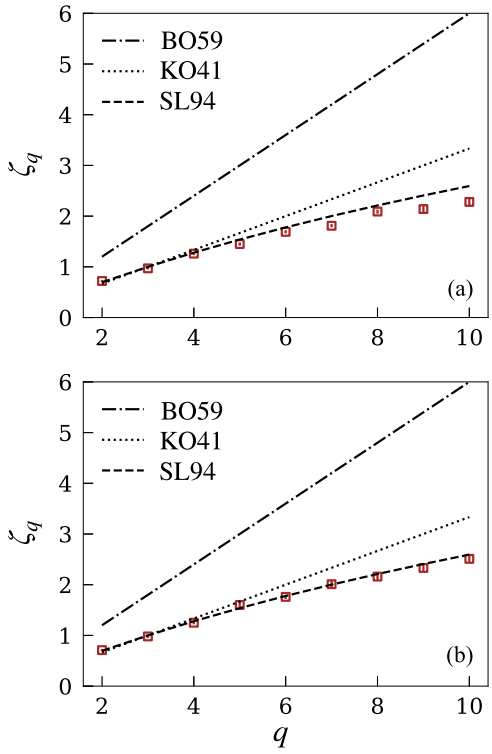

FIG. 4. For (a) the free-slip and (b) no-slip simulations of RBC: plots of ζ_q (squares) vs q. ζ_q matches closely with the predictions of She and Leveque[6] (dashed line). The figures also contain the prediction of Kolmogorov $\zeta_q = q/3$ (dotted line) and the prediction of Bolgiano-Obukhov $\zeta_q = 3q/5$ (chained line).

Interestingly, the aforementioned equation describes ζ_q calculated using our RBC data quite well [see Figs. 4(a) and 4(b)]. These results demonstrate similarities between ζ_q scaling in convection and in hydrodynamic turbulence, consistent with earlier results.[9,10,47] Our results also match with the experimental work of Sun, Zhou, and Xia,[25] who observed the scaling exponents of structure functions calculated at the cell-center to fit with the model of She-Leveque.

In Fig. 5, we plot the logarithms of S_2^u, S_6^u, S_8^u, and S_{10}^u vs $\log_{10}|S_3^u|$ for both free-slip and no-slip cases and observe the structure functions to be self-similar, that is,

$$S_q^u \sim (S_3^u)^{\beta(q,3)}, \tag{37}$$

TABLE II. For the free-slip and no-slip simulations of RBC: prefactor $\mathcal{A}$ and the scaling exponent ζ_q for the structure functions computed by fitting the relation $|S_q^u(l)| = \mathcal{A}l^{\zeta_q}$ to our data.

	Free-slip simulation (Ra = 1.1×10^{11})		No-slip simulation (Ra = 1.0×10^8)	
q	$\mathcal{A}$	ζ_q	$\mathcal{A}$	ζ_q
2	$(2.8 \pm 0.1) \times 10^{-2}$	0.70 ± 0.01	$(2.3 \pm 0.1) \times 10^{-2}$	0.71 ± 0.01
3	$(9.3 \pm 0.5) \times 10^{-4}$	0.97 ± 0.01	$(8.5 \pm 0.5) \times 10^{-4}$	0.98 ± 0.02
4	$(2.0 \pm 0.1) \times 10^{-3}$	1.26 ± 0.02	$(1.6 \pm 0.1) \times 10^{-3}$	1.25 ± 0.02
5	$(1.5 \pm 0.1) \times 10^{-4}$	1.45 ± 0.02	$(2.6 \pm 0.2) \times 10^{-4}$	1.60 ± 0.04
6	$(1.8 \pm 0.1) \times 10^{-4}$	1.69 ± 0.02	$(2.6 \pm 0.2) \times 10^{-4}$	1.76 ± 0.03
7	$(2.1 \pm 0.1) \times 10^{-5}$	1.81 ± 0.02	$(7.6 \pm 0.8) \times 10^{-5}$	2.01 ± 0.05
8	$(2.7 \pm 0.3) \times 10^{-5}$	2.09 ± 0.03	$(6.0 \pm 0.6) \times 10^{-5}$	2.16 ± 0.05
9	$(3.9 \pm 0.7) \times 10^{-6}$	2.14 ± 0.05	$(2.6 \pm 0.4) \times 10^{-5}$	2.33 ± 0.07
10	$(3.1 \pm 0.5) \times 10^{-6}$	2.28 ± 0.05	$(2.1 \pm 0.3) \times 10^{-5}$	2.51 ± 0.07

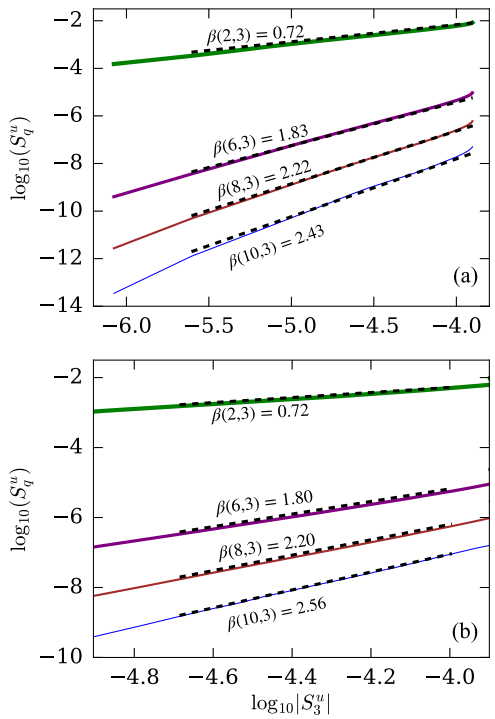

FIG. 5. For (a) the free-slip and (b) no-slip simulations of RBC: plots of S_q^u vs S_3^u. This extended self-similarity goes beyond the inertial range.

where $\beta(q, 3) = \zeta_q/\zeta_3$. The computed values of the exponent $\beta(q, 3)$ are also shown in Fig. 5. This scaling occurs for l/η ranging from 12 to 530 for the free-slip case and 9–45 for the no-slip case. The range of S_q^u vs S_3^u plots of Fig. 5 is wider than that of S_q^u plots of Fig. 3 (in Fig. 5, the range extends well beyond the inertial range to the dissipative scales). This is called extended self-similarity (ESS).[18,19] ESS has been observed in previous studies of convection.[16,17,34] Note that ESS was first reported by Benzi *et al.*[18] in hydrodynamic turbulence.

According to Pope,[62] the upper limit of the inertial range can be estimated by $l_{EI}^P \approx L/6$ and the lower limit $l_{DI}^P \approx 60\eta$. Going by this estimate, $l_{EI}^P = 530\eta$ for our free-slip data. Note that the upper and the lower limits of the power-law range of the structure functions for our free-slip data are of the same order of magnitude as Pope's estimate. For the no-slip case, because of the large value of η and the dissipative nature of the OpenFOAM solver, $l_{DI}^P (= 60\eta)$ is greater than $l_{EI}^P (= 40\eta)$. Therefore, Pope's estimate for the lower limit does not hold for the no-slip case; this is expected because Pope's estimates are expected to work for homogeneous and isotropic turbulence or periodic boundary condition.

An important point to note is that ζ_q curve does not fit with $\zeta_q = 3q/5$, which is a generalization of the Bolgiano-Obukhov (BO) model. As discussed in Sec. III A 2, Kumar, Chatterjee, and Verma[9] and Verma, Kumar, and Pandey[10] have argued against the Bolgiano-Obukhov (BO) model for RBC based on energy flux arguments. This result is contrary to some of the earlier works[12–14,16,17,20,31] that argue in favor of the Bolgiano-Obukhov model. Note that the Bolgiano length computed using $l_B = \mathrm{Nu}^{1/2}/(\mathrm{PrRa})^{1/4}$ is approximately 130η and 14η for the free-slip and no-slip boundary conditions, respectively. They are marked as vertical lines in Fig. 3. We do not discuss l_B in detail because the Bolgiano-Obukhov (BO) model has been shown to be inapplicable for RBC[9,10,47] (see Sec. III A 2).

In the Appendix, we compute the planar structure functions for several horizontal cross sections. We observe that these structure functions are somewhat similar to those described above, with a difference that planar structure functions exhibit relatively higher fluctuations. This is due to lesser averaging for the planar structure function.

In Subsection V B, we describe the probability distribution function (PDF) for the velocity difference between two points.

B. Probability distribution function for velocity increments

For different values of l/η, we compute the probability distribution functions (PDFs) of velocity increments, $\delta u = \{\mathbf{u}(\mathbf{r}+\mathbf{l})-\mathbf{u}(\mathbf{r})\}\cdot\hat{\mathbf{l}}$, using the free-slip and the no-slip data. Figure 6(a) exhibits the PDFs of δu for the free-slip data. For small l, the PDFs are non-Gaussian with wide tails. The tails fit with a stretched exponential curve given by $P(\delta u) \sim \exp(-m|\delta u^*|^\alpha)$, where $\delta u^* = \delta u/\sqrt{\langle \delta u^2\rangle}$. We observe that the stretching exponent $\alpha = 0.8$, 1.0, and 1.8 for $l/\eta = 12$, 62, and 170, respectively. Thus, the PDFs become closer to Gaussian (represented by the dashed black curve) as l increases. This is expected

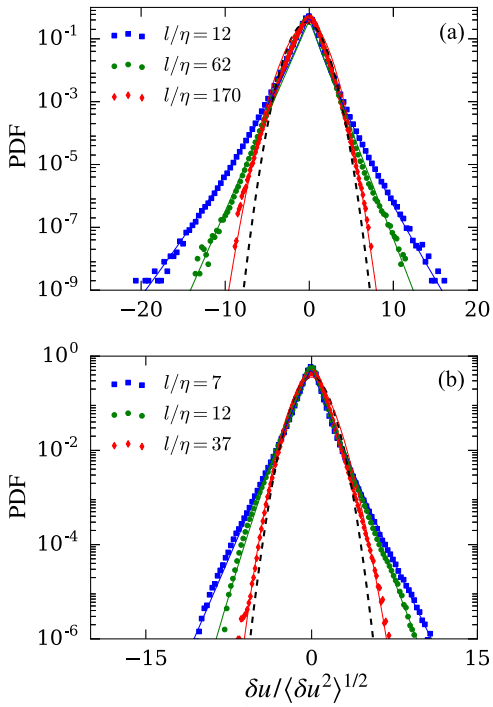

FIG. 6. For (a) the free-slip and (b) no-slip simulations of RBC: probability distribution functions of δu for various l/η (as shown in legends). The tails fit well with the stretched exponential (solid curves). The dashed black curves represent the standard Gaussian distribution.

since the velocities at two largely separated points become independent of each other. Our results are similar to those observed in hydrodynamic turbulence (see Refs. 63 and 64).

Figure 6(b) exhibits the PDFs of δu calculated using the no-slip data. Clearly, the tails are narrower compared to the free-slip case. This is because of the weaker velocity fluctuations owing to the lower Rayleigh number. Moreover, the presence of viscous boundary layers also reduces the fluctuations. Pandey *et al.*[65] showed that for the same parameters, the large scale velocity and heat flux are less for convection with no-slip walls than with free-slip walls. Similar to the free-slip case, the tails of the PDFs fit well with a stretched exponential. For $l/\eta = 7$, 12, and 37, α's are 0.9, 1.0, and 1.7, respectively, for the left tail and 1.0, 1.2, and 1.9, respectively, for the right tail. The PDFs become close to Gaussian at large scales, similar to the free-slip case.

C. Buoyancy forcing, energy flux, and viscous dissipation rate

In this section, we provide a numerical demonstration that the energy flux and the viscous dissipation rate differ in RBC.

Using the third-order velocity structure functions, we calculate the energy flux Π_u using Eq. (32) as

$$\Pi_u = -\frac{5}{4}\frac{S_3^u}{l}. \tag{38}$$

We list the values of the energy flux in Table III. We also compute the Fourier transform of our velocity and temperature field data and compute the spectral energy flux using the following relation:[55,56]

$$\Pi_u(k_0) = \sum_{k\geq k_0}\sum_{p<k_0}\delta_{\mathbf{k},\mathbf{p}+\mathbf{q}}\Im([\mathbf{k}\cdot\mathbf{u}(\mathbf{q})][\mathbf{u}^*(\mathbf{k})\cdot\mathbf{u}(\mathbf{p})]). \tag{39}$$

We plot the flux [computed using Eq. (39)] against k in Fig. 7. We observe the value of the flux to be almost constant in the inertial range, and it closely matches with that computed using Eq. (38). In Table III, we also list the values of ϵ_u computed in Sec. V A.

From Table III, we observe that $\epsilon_u \approx 2\Pi_u$ for the free-slip case and $\approx 3\Pi_u$ for the no-slip case. This is unlike in 3D hydrodynamic turbulence in which the flux and viscous dissipation rate are equal. Our results are consistent with our arguments in Sec. III A 2 where we show that the difference between the flux and the viscous dissipation rate arises due to nonzero buoyancy in the inertial range.

Using the values of $\Pi_u(k)$ computed using Eq. (39), we numerically compute $\frac{d}{dk}\Pi_u(k)$ using the central-difference method. We also compute the energy spectrum $E_u(k)$ and obtain the spectrum of viscous dissipation using the relation $\hat{D}_u(k) = 2\nu k^2 E_u(k)$. Using the values of the dissipation spectrum and $\frac{d}{dk}\Pi_u(k)$ and assuming steady state, we compute $\hat{\mathcal{F}}_B(k)$ using Eq. (17),

$$\hat{\mathcal{F}}_B(k) = \frac{d}{dk}\Pi_u(k) + \hat{D}_u(k).$$

TABLE III. For the two simulations of RBC: energy flux Π_u computed using the third-order structure functions, viscous dissipation rate ϵ_u, and the Kolmogorov constant K_{KO}.

Case	Π_u	ϵ_u	K_{KO}
Free-slip	$(1.29 \pm 0.06)\times 10^{-3}$	2.59×10^{-3}	1.59 ± 0.09
No-slip	$(1.09 \pm 0.03)\times 10^{-3}$	3.18×10^{-3}	1.53 ± 0.04

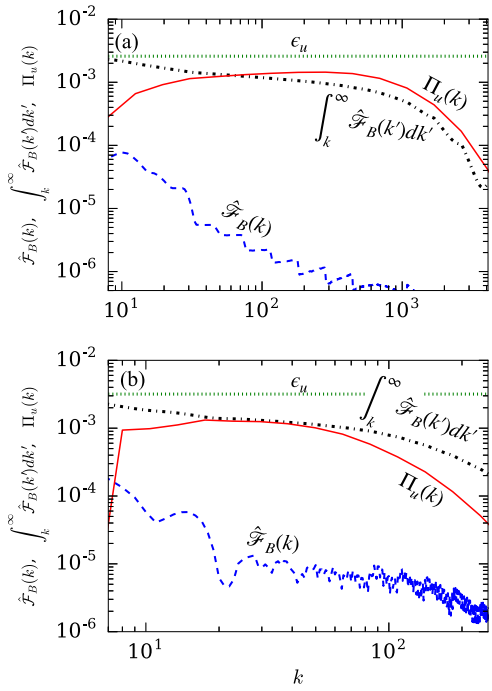

FIG. 7. For (a) the free-slip and (b) no-slip simulations of RBC: the spectra of buoyancy forcing $\hat{\mathcal{F}}_B(k)$ (dashed blue lines), its integral $\int_k^\infty \hat{\mathcal{F}}_B(k')dk'$ (chained black lines), and the kinetic energy flux $\Pi_u(k)$ (solid red lines). $\hat{\mathcal{F}}_B(k)$ is weak in the inertial range. $\Pi_u(k)$ is of the same order as $\int_k^\infty \hat{\mathcal{F}}_B(k')dk'$ and is less than the viscous dissipation rate ϵ_u (dotted green lines).

We plot the values of $\Pi_u(k)$, $\hat{\mathcal{F}}_B(k)$, and $\int_k^\infty \hat{\mathcal{F}}_B(k')dk'$ in Fig. 7(a) for the free-slip case and in Fig. 7(b) for the no-slip case. In each of the plots, we also draw a horizontal line denoting the viscous dissipation rate. As shown in Figs. 7(a) and 7(b), in the inertial range,

$$\Pi_u \sim \int_k^\infty \hat{\mathcal{F}}_B(k')dk'$$

and is approximately $\epsilon_u/2$ for the free-slip case and $\epsilon_u/3$ for the no-slip case. In addition, $\hat{\mathcal{F}}_B(k')$ in the inertial range is weak, consistent with our previous arguments.

In Fig. 8, we plot the cumulative buoyant energy forcing $\int_0^k \hat{\mathcal{F}}_B(k')dk'$, the cumulative viscous dissipation rate $\int_0^k \hat{D}_u(k')dk'$, and the energy flux $\Pi_u(k)$ against k for both sets of data. The plots clearly show that the cumulative buoyant energy forcing at small wavenumbers contributes to the energy flux in the inertial range, consistent with our arguments in Sec. III A 2. For the free-slip data, $\int_0^k \hat{\mathcal{F}}_B(k')dk'$ remains close to the flux until $k = 200$, after which it deviates from $\Pi_u(k)$. Similar behavior is also observed for the no-slip data, but with the threshold wavenumber $k = 18$. Above these wavenumbers, $\int_0^k \hat{\mathcal{F}}_B(k')dk'$ increases slowly and merges with the

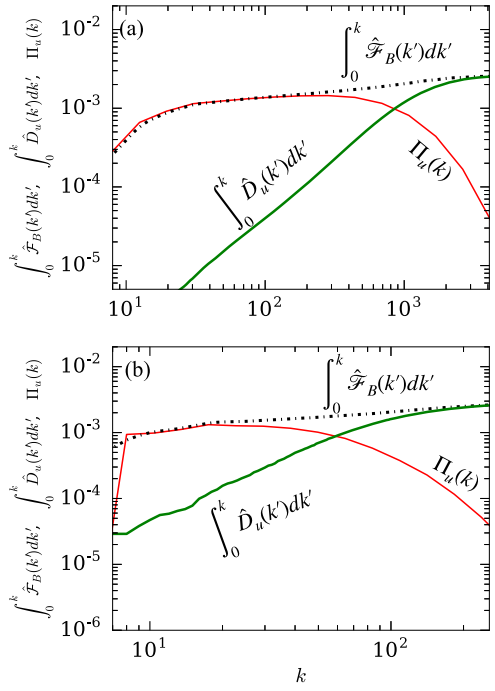

FIG. 8. For (a) the free-slip and (b) no-slip simulations of RBC: the spectra of cumulative buoyancy forcing $\int_0^k \hat{\mathcal{F}}_B(k')dk'$ (chained black lines), kinetic energy flux $\Pi_u(k)$ (solid red lines), and cumulative dissipation rate $\int_0^k \hat{D}_u(k')dk'$ (thick green lines). The cumulative buoyancy forcing at small wavenumbers contributes mainly to the flux in the inertial range.

cumulative dissipation rate $\int_0^k \hat{D}_u(k')dk'$ at dissipation wavenumbers. It is clear that $\int_0^k \hat{\mathcal{F}}_B(k')dk'$ at small wavenumbers (which contributes to the inertial range energy flux) is, respectively, 1/2 and 1/3 of the total energy injection rate $[\int_0^\infty \hat{\mathcal{F}}_B(k')dk']$ for the free-slip and the no-slip data.

Finally, we compute the Kolmogorov constant K_{KO} by first calculating the constant C using the following relation involving the second-order structure function and the energy flux:

$$S_2^u(l) = C(\Pi_u)^{2/3} l^{2/3}. \tag{40}$$

After this, we compute the Kolmogorov constant using[62]

$$K_{\mathrm{KO}} = \frac{55}{72} C. \tag{41}$$

We list the values of Kolmogorov constant for both free-slip and no-slip cases in Table III. Interestingly, K_{KO} of Table III is quite close to that for hydrodynamic turbulence.[3]

VI. CONCLUSIONS

Using the numerical data of thermal convection, we compute the velocity structure functions S_q^u for $q = 2$–10. The first dataset[10] was generated with free-slip boundary conditions for Ra = 1.1×10^{11} and Pr = 1, and the second set[57] with no-slip boundary conditions with Ra = 1×10^8 and Pr = 1. We calculate the scaling exponent ζ_q from S_q^u.

We show that the third-order structure functions, computed using both sets of data, scale according to Kolmogorov's theory $[S_3^u = -(4/5)\Pi_u l]$. Our results are consistent with Kolmogorov's energy spectrum observed in turbulent convection. The exponents of the structure functions of thermal convection match well with the predictions of She-Leveque. We demonstrate that the structure functions show extended self-similarity.

We also calculate the probability distribution function (PDF) of velocity increments for different values of the separation distance l. We show that for small l, the PDFs are non-Gaussian with wide tails. With increasing l, the PDFs become closer to Gaussian. The tails of the PDFs follow a stretched exponential, and the stretching exponent increases with l. Note that the PDFs of hydrodynamic turbulence show similar behavior.

We compute the energy flux Π_u using the third-order structure functions and show that $\Pi_u \neq \epsilon_u$; instead, it is two to three times less than ϵ_u for our cases. This is unlike in hydrodynamic turbulence where flux equals the dissipation rate. Using phenomenological arguments, we have shown that this difference arises due to nonzero, albeit weak, buoyancy present in the inertial range.

In summary, the scaling behavior of velocity structure functions of turbulent convection shows similarities with those of 3D hydrodynamic turbulence. We do not analyze the temperature structure functions in this paper. Some of the notable works on temperature structure functions of turbulent convection include those of Ching[20] and Ching *et al.*[26] We will discuss the scaling of temperature structure functions in a future work.

ACKNOWLEDGMENTS

We are grateful to A. Kumar and A. Chatterjee for sharing their numerical data with us. We acknowledge R. Samuel and M. Sharma for their contributions in the development of the code to calculate structure functions. We thank S. Chakraborty and S. Vashishtha for useful discussions. Our numerical simulations were performed on Shaheen II at KAUST Supercomputing Laboratory, Saudi Arabia, under project No. k1052. This work was supported by Research Grant No. PLANEX/PHY/2015239 from Indian Space Research Organisation, India, and the Department of Science and Technology, India (Grant No. INT/RUS/RSF/P-03) for the Indo-Russian project.

APPENDIX: EXTENT OF HOMOGENEITY IN TURBULENT CONVECTION

For very high Rayleigh number RBC, the boundary layers are quite thin. Hence, the flow, mostly residing in the bulk, is nearly homogeneous. However, for relatively smaller Ra (around 10^8), there can be some inhomogeneity due to plumes and large-scale structures. To test the extent of inhomogeneity, we compute the third-order velocity structure functions for three horizontal slices of the free-slip and no-slip flow profiles detailed in the main text. The three slices are at $z = 0.25$, 0.5, and 0.75. Note that the $z = 0.5$ corresponds to the midplane.

Figure 9 exhibits the plots of $|S_3^u(l)|$ vs l/η for the three planes. For the free-slip data with higher Ra [Fig. 9(a)], $|S_3^u(l)| \sim l^{\zeta_3}$, where $\zeta_3 \approx 1$ for $z = 0.25$ and 0.5. However, for the $z = 0.75$ plane,

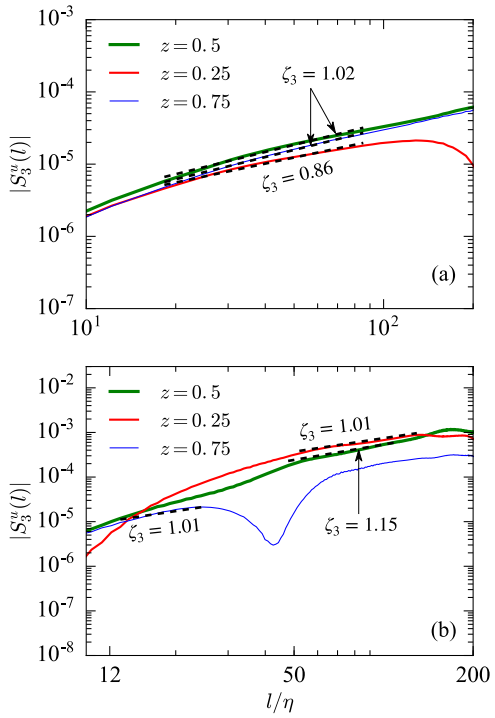

FIG. 9. Plots of the planar structure function $S_3^u(l)$ at z = 0.25, 0.5, and 0.75 for (a) the free-slip and (b) no-slip simulations. Despite some spatial inhomogeneity, especially for the no-slip boundary condition (b), there exists scaling range with the scaling exponent $\zeta_3 \sim 1$.

$\zeta_3 = 0.86$, which is slightly below unity. The upper and the lower limits of the scaling range are nearly the same as those for the structure functions computed in the entire domain [see Fig. 3(a)]. Thus, it is reasonable to assume the free-slip data to be homogeneous. However, we observe stronger spatial inhomogeneities for the no-slip data, as shown in Fig. 9(b). Here, the scaling regime of $|S_3^u(l)| \sim l^{\zeta_3}$ is observed for all three planes, with ζ_3 ranging from 1.02 to 1.15. However, the range of the scaling regime differs for the three planes. Note that the spatial inhomogeneities are stronger for no-slip boundary conditions due to the relatively stronger plumes for the no-slip boundaries.

As mentioned earlier, the observed inhomogeneity, which is more prominent for no-slip data, can be attributed to localized plumes. Thus, the structure functions are required to be averaged over more points to cancel out the effects of the plumes. That is why bulk structure functions are smoother than those for the planes, and they are closer to the predictions of She-Leveque.[6]

REFERENCES

[1] A. N. Kolmogorov, "Dissipation of energy in locally isotropic turbulence," Dokl. Akad. Nauk SSSR **32**, 16–18 (1941).

[2] A. N. Kolmogorov, "The local structure of turbulence in incompressible viscous fluid for very large Reynolds numbers," Dokl. Akad. Nauk SSSR **30**, 301–305 (1941).

[3] U. Frisch, *Turbulence: The Legacy of A. N. Kolmogorov* (Cambridge University Press, Cambridge, 1995).

[4] A. M. Obukhov, "Structure of the temperature field in a turbulent flow," Isv. Geogr. Geophys. Ser. **13**, 58–69 (1949).

[5] S. Corrsin, "On the spectrum of isotropic temperature fluctuations in an isotropic turbulence," J. Appl. Phys. **22**, 469–473 (1951).

[6] Z.-S. She and E. Leveque, "Universal scaling laws in fully developed turbulence," Phys. Rev. Lett. **72**, 336–339 (1994).

[7] R. Bolgiano, "Turbulent spectra in a stably stratified atmosphere," J. Geophys. Res. **64**, 2226–2229, https://doi.org/10.1029/jz064i012p02226 (1959).

[8] A. M. Obukhov, "On influence of buoyancy forces on the structure of temperature field in a turbulent flow," Dokl. Akad. Nauk SSSR **125**, 1246 (1959).

[9] A. Kumar, A. G. Chatterjee, and M. K. Verma, "Energy spectrum of buoyancy-driven turbulence," Phys. Rev. E **90**, 023016 (2014).

[10] M. K. Verma, A. Kumar, and A. Pandey, "Phenomenology of buoyancy-driven turbulence: Recent results," New J. Phys. **19**, 025012 (2017).

[11] D. L. Rosenberg, A. G. Pouquet, R. Marino, and P. D. Mininni, "Evidence for Bolgiano-Obukhov scaling in rotating stratified turbulence using high-resolution direct numerical simulations," Phys. Fluids **27**, 055105 (2015).

[12] I. Procaccia and R. Zeitak, "Scaling exponents in nonisotropic convective turbulence," Phys. Rev. Lett. **62**, 2128–2131 (1989).

[13] V. S. L'vov, "Spectra of velocity and temperature-fluctuations with constant entropy flux of fully-developed free-convective turbulence," Phys. Rev. Lett. **67**, 687–690 (1991).

[14] V. S. L'vov and G. Falkovich, "Conservation laws and two-flux spectra of hydrodynamic convective turbulence," Physica D **57**, 85–95 (1992).

[15] R. Rubinstein, "Renormalization group theory of Bolgiano scaling in Boussinesq turbulence," Technical Report ICOM-94-8; CMOTT-94-2, 1994.

[16] R. Benzi, F. Massaioli, S. Succi, and R. Tripiccione, "Scaling behaviour of the velocity and temperature correlation functions in 3D convective turbulence," Europhys. Lett. **28**, 231–236 (1994).

[17] R. Benzi, R. Tripiccione, F. Massaioli, S. Succi, and S. Ciliberto, "On the scaling of the velocity and temperature structure functions in Rayleigh-Bénard convection," Europhys. Lett. **25**, 341–346 (1994).

[18] R. Benzi, S. Ciliberto, R. Tripiccione, C. Baudet, F. Massaioli, and S. Succi, "Extended self-similarity in turbulent flows," Phys. Rev. E **48**, R29–R32 (1993).

[19] S. Chakraborty, U. Frisch, and S. S. Ray, "Extended self-similarity works for the Burgers equation and why," J. Fluid Mech. **649**, 275–285 (2010).

[20] E. S. C. Ching, "Intermittency of temperature field in turbulent convection," Phys. Rev. E **61**, R33 (2000).

[21] F. Heslot, B. Castaing, and A. Libchaber, "Transitions to turbulence in helium gas," Phys. Rev. A **36**, 5870–5873 (1987).

[22] M. Sano, X.-Z. Wu, and A. Libchaber, "Turbulence in helium-gas free convection," Phys. Rev. A **40**, 6421–6430 (1989).

[23] R. Benzi, L. Biferale, S. Ciliberto, M. Struglia, and R. Tripiccione, "Generalized scaling in fully developed turbulence," Physica D **96**, 162–181 (1996).

[24] E. Calzavarini, F. Toschi, and R. Tripiccione, "Evidences of Bolgiano-Obhukhov scaling in three-dimensional Rayleigh-Bénard convection," Phys. Rev. E **66**, 016304 (2002).

[25] C. Sun, Q. Zhou, and K.-Q. Xia, "Cascades of velocity and temperature fluctuations in buoyancy-driven thermal turbulence," Phys. Rev. Lett. **97**, 144504 (2006).

[26] E. S. C. Ching, Y.-K. Tsang, T. N. Fok, X. He, and P. Tong, "Scaling behavior in turbulent Rayleigh-Bénard convection revealed by conditional structure functions," Phys. Rev. E **87**, 013005 (2013).

[27] X. He and P. Tong, "Measurements of the thermal dissipation field in turbulent Rayleigh-Bénard convection," Phys. Rev. E **79**, 026306 (2009).

[28] B. Castaing, G. Gunaratne, L. P. Kadanoff, A. Libchaber, and F. Heslot, "Scaling of hard thermal turbulence in Rayleigh-Bénard convection," J. Fluid Mech. **204**, 1–30 (1989).

[29] X.-D. Shang, X.-L. Qiu, P. Tong, and K.-Q. Xia, "Measured local heat transport in turbulent Rayleigh-Bénard convection," Phys. Rev. Lett. **90**, 074501 (2003).

[30] E. S. C. Ching, "Scaling laws in the central region of confined turbulent thermal convection," Phys. Rev. E **75**, 056302 (2007).

[31] R. P. J. Kunnen, H. J. H. Clercx, B. J. Geurts, L. J. A. van Bokhoven, R. A. D. Akkermans, and R. Verzicco, "Numerical and experimental investigation of

structure-function scaling in turbulent Rayleigh-Bénard convection," Phys. Rev. E **77**, 016302 (2008).
[32]E. S. C. Ching and W. C. Cheng, "Anomalous scaling and refined similarity of an active scalar in a shell model of homogeneous turbulent convection," Phys. Rev. E **77**, 015303 (2008).
[33]M. Kaczorowski and K.-Q. Xia, "Turbulent flow in the bulk of Rayleigh–Bénard convection: Small-scale properties in a cubic cell," J. Fluid Mech. **722**, 596–617 (2013).
[34]D. Lohse and K.-Q. Xia, "Small-scale properties of turbulent Rayleigh–Bénard convection," Annu. Rev. Fluid Mech. **42**, 335–364 (2010).
[35]T. Meuel, M. Coudert, P. Fischer, C. Bruneau, and H. Kellay, "Effects of rotation on temperature fluctuations in turbulent thermal convection on a hemisphere," Sci. Rep. **8**, 16513 (2018).
[36]A. Alexakis and L. Biferale, "Cascades and transitions in turbulent flows," Phys. Rep. **767-769**, 1–101 (2018).
[37]C. Bruneau, P. Fischer, Y.-L. Xiong, and H. Kellay, "Numerical simulations of thermal convection on a hemisphere," Phys. Rev. Fluids **3**, 043502 (2018).
[38]A. Shestakov, R. Stepanov, and P. Frick, "On cascade energy transfer in convective turbulence," J. Appl. Mech. Tech. Phys. **58**, 1171 (2017).
[39]S. S. Pawar and J. H. Arakeri, "Kinetic energy and scalar spectra in high Rayleigh number axially homogeneous buoyancy driven turbulence," Phys. Fluids **28**, 065103 (2016).
[40]J. K. Bhattacharjee, "Kolmogorov argument for the scaling of the energy spectrum in a stratified fluid," Phys. Lett. A **379**, 696–699 (2015).
[41]J. Schumacher, P. Götzfried, and J. D. Scheel, "Enhanced enstrophy generation for turbulent convection in low-Prandtl-number fluids," Proc. Natl. Acad. Sci. U. S. A. **112**, 9530 (2015).
[42]K. Shrestha, G. Mompean, and E. Calzavarini, "Finite-volume versus streaming-based lattice Biltzmann algorithm for fluid-dynamics simulations: A one-to-one accuracy and performance study," Phys. Rev. E **93**, 023306 (2016).
[43]F. Rincon, T. Roudier, A. Schekochihin, and M. Rieutord, "Supergranulation and multiscale flows in the solar photosphere," Astron. Astrophys. **599**, A69 (2017).
[44]F. Rincon and M. Rieutord, "The Sun's supergranulation," Living Rev. Sol. Phys. **15**, 6 (2018).
[45]S. Chandrasekhar, *Hydrodynamic and Hydromagnetic Stability* (Oxford University Press, Oxford, 2013).
[46]F. Chillà and J. Schumacher, "New perspectives in turbulent Rayleigh-Bénard convection," Eur. Phys. J. E **35**, 58 (2012).
[47]M. K. Verma, *Physics of Buoyant Flows* (World Scientific, Singapore, 2018).
[48]M. Lesieur, *Turbulence in Fluids* (Springer-Verlag, Dordrecht, 2008).
[49]C. Canuto, M. Y. Hussaini, A. Quarteroni, and T. A. Zang, *Spectral Methods in Fluid Dynamics* (Springer-Verlag, Berlin, Heidelberg, 1988).
[50]A. Pandey and M. K. Verma, "Scaling of large-scale quantities in Rayleigh-Bénard convection," Phys. Fluids **28**, 095105 (2016).
[51]A. Pandey, A. Kumar, A. G. Chatterjee, and M. K. Verma, "Dynamics of large-scale quantities in Rayleigh-Bénard convection," Phys. Rev. E **94**, 053106 (2016).
[52]D. Nath, A. Pandey, A. Kumar, and M. K. Verma, "Near isotropic behavior of turbulent thermal convection," Phys. Rev. Fluids **1**, 064302 (2016).
[53]Q. Zhou, C. Sun, and K.-Q. Xia, "Experimental investigation of homogeneity, isotropy, and circulation of the velocity field in buoyancy-driven turbulence," J. Fluid Mech. **598**, 361–372 (2008).
[54]R. P. J. Kunnen and H. J. H. Clercx, "Probing the energy cascade of convective turbulence," Phys. Rev. E **90**, 063018 (2014).
[55]M. K. Verma, A. G. Chatterjee, R. K. Yadav, S. Paul, M. Chandra, and R. Samtaney, "Benchmarking and scaling studies of pseudospectral code Tarang for turbulence simulations," Pramana **81**, 617–629 (2013).
[56]A. G. Chatterjee, M. K. Verma, A. Kumar, R. Samtaney, B. Hadri, and R. Khurram, "Scaling of a fast Fourier transform and a pseudo-spectral fluid solver up to 196608 cores," J. Parallel Distrib. Comput. **113**, 77–91 (2018).
[57]A. Kumar and M. K. Verma, "Applicability of Taylor's hypothesis in thermally driven turbulence," R. Soc. Open Sci. **5**, 172152 (2018).
[58]H. Jasak, A. Jemcov, Z. Tukovic *et al.*, "OpenFOAM: A C++ library for complex physics simulations," in *International Workshop on Coupled Methods in Numerical Dynamics* (IUC, Dubrovnik, Croatia, 2007), Vol. 1000, pp. 1–20.
[59]S. Bhattacharya, A. Pandey, A. Kumar, and M. K. Verma, "Complexity of viscous dissipation in turbulent thermal convection," Phys. Fluids **30**, 031702 (2018).
[60]S. Bhattacharya, R. Samtaney, and M. K. Verma, "Scaling and spatial intermittency of thermal dissipation in turbulent convection," Phys. Fluids **31**, 075104 (2019).
[61]P. S. Pacheco, *An Introduction to Parallel Programming* (Morgan Kaufmann, Burlington, 2011).
[62]S. B. Pope, *Turbulent Flows* (Cambridge University Press, Cambridge, 2000).
[63]P. Kailasnath, K. R. Sreenivasan, and G. Stolovitzky, "Probability density of velocity increments in turbulent flows," Phys. Rev. Lett. **68**, 2766–2769 (1992).
[64]D. A. Donzis, P. K. Yeung, and K. R. Sreenivasan, "Dissipation and enstrophy in isotropic turbulence: Resolution effects and scaling in direct numerical simulations," Phys. Fluids **20**, 045108 (2008).
[65]A. Pandey, M. K. Verma, A. G. Chatterjee, and B. Dutta, "Similarities between 2D and 3D convection for large Prandtl number," Pramana **87**, 13 (2016).